Materials Chemistry and Physics 137 (2012) 372–380

Contents lists available at SciVerse ScienceDirect

Materials Chemistry and Physics

journal homepage: www.elsevier.com/locate/matchemphys

Characterizing individual SnO_2 nanobelt field-effect transistors and their intrinsic responses to hydrogen and ambient gases

Yi Cheng [a,*], Rusen Yang [b,1], Jian-Ping Zheng [c], Zhong Lin Wang [b], Peng Xiong [a]

[a] Department of Physics and Integrative NanoScience Institute, Florida State University, Tallahassee, FL 32306, USA
[b] School of Materials Science and Engineering, Georgia Institute of Technology, Atlanta, GA 30332, USA
[c] Department of Electrical and Computer Engineering, College of Engineering, Florida A&M University and Florida State University, Tallahassee, FL 32310, USA

HIGHLIGHTS

- We characterize the intrinsic electrical properties of single SnO_2 nanobelt.
- We report field-effect transistor (FET) devices based on single SnO_2 nanobelt.
- We report room temperature hydrogen gas sensing with proposed transduction mechanism.
- We report ambient gas dependent mobility and carrier concentration of SnO_2 nanobelt.

GRAPHICAL ABSTRACT

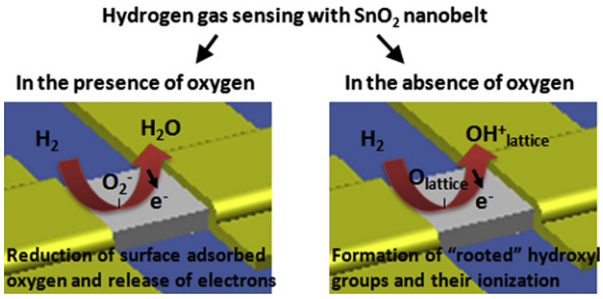

ARTICLE INFO

Article history:
Received 8 November 2011
Received in revised form
28 August 2012
Accepted 23 September 2012

Keywords:
Oxides
Nanostructures
Chemisorption
Electrical properties
Surface properties

ABSTRACT

The intrinsic electrical properties of individual single-crystalline tin dioxide nanobelts, synthesized via catalyst-free physical vapor deposition, were studied and correlated to the surface oxygen deficiency with the presence of various ambient gases, especially hydrogen. Four-terminal field-effect transistor (FET) devices based on individual SnO_2 nanobelts were fabricated with SiO_2/Si as back gate and RuO_2/Au as contacts. Four-probe I–V measurements verify channel-limited transistor characteristics and ensure that the hydrogen gas sensing reflect electrical modification of the nanobelt channel. The demonstrated results of the intrinsic SnO_2 nanobelt based hydrogen sensor operating at room temperature provide useful information on the synthesis of room temperature chemo-resistive gas sensors with good sensitivity and stability. To evaluate the impact of surface gas composition on the electrical properties of SnO_2 nanobelts, their temperature-dependent resistivity (ρ), effective carrier mobility (μ_{eff}) and effective carrier concentration (n_e) were determined under different oxygen concentrations.

1. Introduction

Due to their tunable composition, unique geometry, large surface-to-volume ratio, and their intrinsic surface chemistry, quasi one-dimensional (Q1D) metal oxide nanostructures have been used as active components in the electronic [1]and gas sensing devices [2–5]. Several metal oxide nanomaterials, such as ZnO, SnO_2, and In_2O_3, have been synthesized [3,6–10] and demonstrate gas-sensing functionalities [2–5,11–13]. Solid-state metal oxide semiconductor gas sensors have a high portablization potential as they

* Corresponding author. Current address: Department of Materials Science and Engineering & Institute for Systems Research, University of Maryland, College Park, MD 20742, USA. Tel.: +1 301 405 2971.
E-mail address: cheng@umd.edu (Y. Cheng).
[1] Current address: Department of Mechanical Engineering, University of Minnesota, Minneapolis, MN 55455, USA.

0254-0584/$ – see front matter © 2012 Elsevier B.V. All rights reserved.
http://dx.doi.org/10.1016/j.matchemphys.2012.09.037

do not require additional optical or spectroscopic components [14]. Among them, SnO_2 is of particular interest for metal-oxide-based solid-state gas sensing devices based on its surface sensitivity to adsorbents of oxidizing and reducing gases. Tremendous efforts have been devoted to developing SnO_2 nanostructures with the goal of producing a new generation of high-performance devices including electronic devices [1,15,16], gas sensors [11,17–19] and biosensors [20–22]. Compared with conventional powder-compact or thin-film type SnO_2 gas sensors, Q1D nanomaterials are expected to have a higher sensitivity due to their large active surface and the fact that their lateral dimension is comparable to the width of the surface space charge region [23]. However, most of the previous studies on hydrogen sensor were based on two-terminal devices and often at an elevated temperature. The Schottky barriers at metal/semiconductor junctions [24] rather than the semiconductor channel could dominate the electrical transport properties of the device [25,26]. For quantitative and scalable sensing applications, it is important to establish that the signal comes predominantly from the modulation of the SnO_2 rather than the contacts. Therefore, four-terminal devices with standard four-probe measurement [24] are necessary to confirm the gas-sensing mechanism and ensure the oxide entity as the origin of the sensor responses. Moreover, the long term stability at the operating temperature (typically 250–600 °C) of these highly sensitive materials composed of oxide components is still challenging (e.g. grain growth during heat treatment) [27]. Identifying the intrinsic electrical response of the SnO_2 nanobelt to hydrogen at room temperature would benefit the development of chemo-resistive gas sensor at low operating temperatures.

In this paper, we report the construction of individual SnO_2 nanobelts field-effect transistor with low resistance, four-terminal, Ohmic contacts and their application as a room-temperature hydrogen gas sensor. Their reversible, intrinsic responses to hydrogen gas at room temperature are demonstrated and compared with different recovering gases (ambient air and nitrogen). We quantified the transistor performance at different ambient oxygen concentrations and correlated the channel conduction states with the level of oxygen deficiency (stoichiometry) of the nanobelts. Consequently, the effective carrier concentrations and mobility at different partial oxygen concentrations were reliably deduced from the corresponding threshold voltages (V_{th}) and transconductance (g_m) of the SnO_2 nanobelt FET device.

2. Experimental section

The SnO_2 nanobelts were synthesized catalyst-free using the physical vapor deposition (PVD) method under controlled conditions [6]. In a typical experiment, single crystalline SnO_2 nanobelts were synthesized by thermal evaporation of either SnO_2 powders at 1350 °C or SnO powders at 1000 °C that were loaded on an alumina boat in the middle of a horizontal tube furnace under 200 Torr pressure and 50 sccm Ar gas flow for 2 h. The resulting SnO_2 nanobelts are single-crystalline (rutile (101) plane) and have widths of a few hundred nanometers, thicknesses of less than 100 nm and lengths as long as a few hundred micrometers. Fig. 1a shows a SEM picture of bundles of SnO_2 nanobelts grown on an alumina substrate. The typical resistivity of the SnO_2 nanobelts at room temperature in ambient air is around 2.0 Ω cm. The fabrication procedure for SnO_2 nanobelt FET sensors has been described previously [28]. Briefly, SnO_2 nanobelts in a wool-like bundle were first separated by ultrasound agitation in an isopropanol alcohol solution. Then, the nanobelts were dispersed onto the substrate by dripping the solution onto the substrate. In this case, the substrate is a degeneratively doped Si (100) wafer (n-type, Sb dopant, $\rho \sim 1$ mΩ cm, $n \sim 10^{19}$ cm^{-3}, Silicon Quest International) with a 250 nm thermally grown oxide layer on top. Post-annealing (96 °C) and dehydrating were performed in order to remove the leftover solvent and improve the nanobelt/SiO_2 interface, which is critical for the effective enhancement of gate bias modulation and minimizing electron scattering at the interface between the channel and the dielectric layer in the FETs. An individual nanobelt was then identified and contacted using a multi-terminal electrode

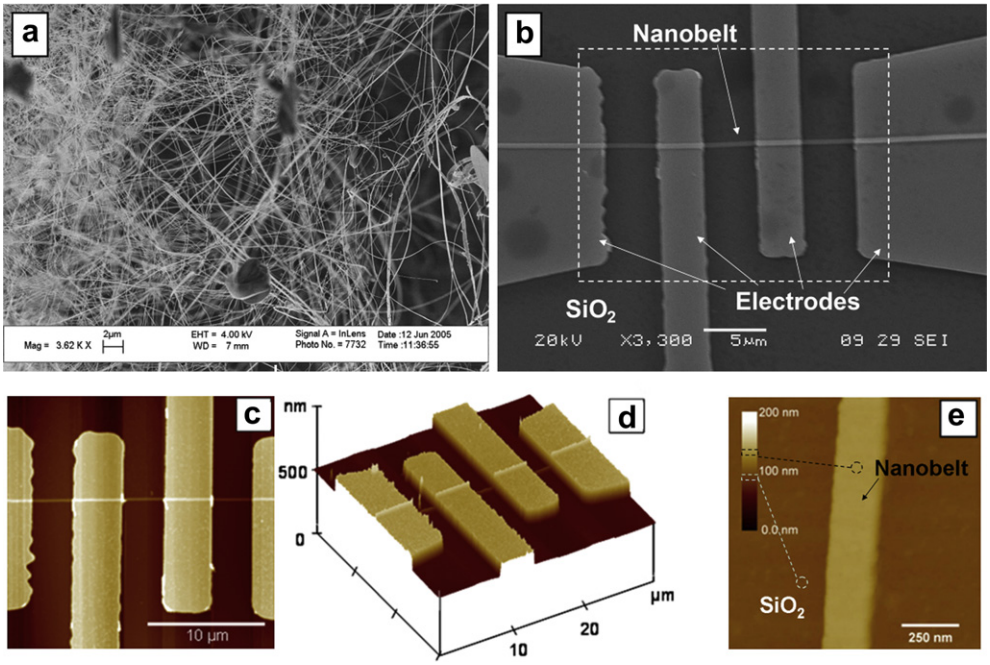

Fig. 1. (a) A SEM micrograph of a SnO_2 nanobelt bundle grown by the PVD method. (b) A SEM micrograph of a SnO_2 nanobelt FET device with four RuO_2/Au electrodes contacting the single SnO_2 nanobelt. (c) 2D and (d) 3D AFM topography micrographs of the central area of the device, indicated by a white dashed rectangle in Fig. 1b. (e) An AFM topography micrograph of part of the SnO_2 nanobelt on the SiO_2 substrate surface.

produced by photolithography and thermal evaporation (for metal contacts) or pulsed laser ablation (for RuO_2 contacts) and lift-off. Fig. 1b presents a SEM micrograph of a single SnO_2 nanobelt FET. The single nanobelt is lying on a SiO_2 substrate and contacted by four RuO_2/Au electrodes. Fig. 1c–e show AFM micrographs illustrating the structure and dimensions of the device and the nanobelt. Fig. 1c is a 2D topography of the central area (indicated with white dashed rectangle in Fig. 1b) of the nanobelt FET device. Fig. 1d is a 3D topography of the same area described in Fig. 1c. Fig. 1e is the topography scan of the nanobelt showing the belt-like morphology with a width of 219 nm and a thickness of 38 nm.

Unlike most 2-probe devices where source and drain are the only electrodes interconnected by the nanobelt, here we used a 4-probe (Fig. 1b) configuration to determine the contact resistance (R_C). As shown in Fig. 1b, in our configuration, the active channel of the transistor is actually the central part of the nanobelt between the two middle electrodes (Fig. 1b). The contact resistance is determined by comparing the resistance values of the 4-probe (R_{4P}) and the 2-probe (R_{2P}), and it is two orders of magnitude smaller than the actual nanobelt resistance (details in Section 3.1 and in Fig. 2).

Transistor measurements were performed using a home-built probe station equipped with a Keithley 4200-SCS semiconductor characterization system. The gas sensing experiments were carried out using a quartz tube in a furnace for temperature control; electrical and gas feedthroughs on a compression fitting were used for electrical measurements and gas flow respectively.

3. Results and discussion

3.1. Making Ohmic contacts to single SnO_2 nanobelt

Metal/semiconductor contact is a technically important and rather complicated issue that has been investigated extensively [29–33]. There are two major types of metal/semiconductor contacts: Ohmic and Schottky. For an n-type semiconductor, ideally the contact barrier height Φ_b at the metal/semiconductor junction, defined as the difference between the bottom of the semiconductor conduction band and the metal Fermi level at the junction, is [34]

$$e\Phi_b = e\Phi_m - e\chi_s \quad (1)$$

where e is the electron charge, Φ_b is the contact barrier height, Φ_m is the metal work function, χ_s is the electron affinity of a semiconductor. The electrons coming from the semiconductor into the metal face a barrier (denoted by eV_{bi}) called the built-in potential of the junction. It is determined by the work function difference between semiconductor Φ_s and the contact metal Φ_m [34].

$$eV_{bi} = e\Phi_m - e\Phi_s \quad (2)$$

Thus, when low work function metals like Cr (4.50 eV) or Ti (3.84 eV) are brought into contact with SnO_2, whose work function is about 7.74 eV [35] and electron affinity is around 4.8 eV, the junctions are expected to be Ohmic [36]. However, direct metallization with Cr/Au and Ti/Au on SnO_2 nanobelts often results in poor electrical contacts, possibly due to metal oxidation or surface chemical impurities/organic residue at the SnO_2/metal interface (detail in Supplementary data Section 1). On the other hand, we consistently obtain good Ohmic contacts with pulsed laser deposition of RuO_2 (~200 nm) at room temperature [37,38], followed by a layer of Au (~100 nm) via thermal evaporation, which was used to facilitate wire bonding. Consistent formation of Ohmic contacts here is likely due to the metallic behavior of RuO_2 (work function of 5.1 eV [39,40]) and the limitations of interfacial diffusion and reaction at the SnO_2/RuO_2 interface.

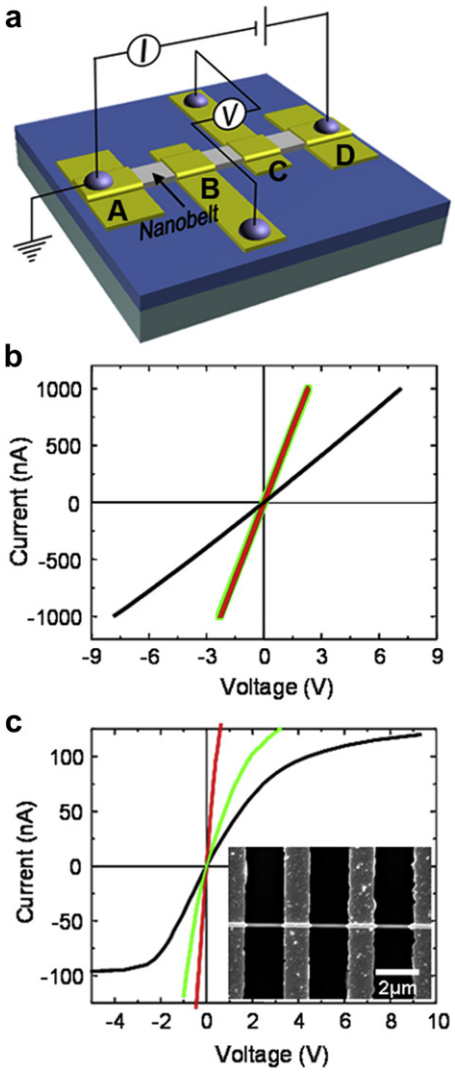

Fig. 2. (a) A schematic circuit diagram for the standard 4-probe I–V measurements on a FET device with four contact electrodes. (b) 2-Probe and 4-probe I–V curves for a SnO_2 nanobelt with low resistance Ohmic contacts (RuO_2/Au). (c) 2-Probe and 4-probe I–V curves for a SnO_2 nanobelt with high resistance Schottky contacts (Ti/Au). Inset, a SEM micrograph of a SnO_2 nanobelt with four-terminal Ti/Au contacts. In both (b) and (c), the red curve represents the 4-probe BC, the green curve represents the 2-probe BC and the black curve represents the 2-probe AD (For interpretation of the references to color in this figure legend, the reader is referred to the web version of this article.).

Making Ohmic electrical contacts to individual SnO_2 nanobelts is an important step toward rigorous characterization of their intrinsic responses as gas sensors. As discussed in the review article by Göpel and Schierbaum [25], the configuration of the sensor can lead to systems where the sensor resistance is dominated by one type of contact, such as the electrode/SnO_2 interface. At the first stage, the difference between the Schottky barrier contact and the low resistance Ohmic contact can be distinguished by comparing the 4-probe and 2-probe I–V measurements (Fig. 2). Fig. 2a depicts the circuit diagrams for standard 4-probe I–V measurements of the nanobelt. For standard 4-probe I–V measurements, we injected current through terminals A and D, and measured the voltage between terminals B and C. 2-Probe I–V measurements were also carried out between terminals BC and terminals AD separately. Fig. 2b and c shows the comparison of the 4-probe and the 2-probe I–V characteristics of one device with Ohmic contacts and another device with Schottky contacts. The red curve represents the voltage

reading between terminals B and C when current flows from terminal A to D. The green curve represents the voltage reading between terminal B and C when current flows through the same terminals. The black curve represents the voltage reading between terminals A and D when current flows through the same terminals (For interpretation of the references to color in this paragraph, the reader is referred to the web version of this article.).

Fig. 2b shows the 4-probe and 2-probe (two center contacts) I–V characteristics of a SnO_2 nanobelt device with four RuO_2/Au Ohmic contacts. Both I–V curves are linear and the contact resistance is less than 1% of the channel resistance. The ratio of resistances between terminals BC and AD is about the same as that of the active lengths between the corresponding terminals, which attests to the uniformity and consistency of the resistivity along the entire length of the nanobelt. The average contact resistance for all of our devices with Ohmic contacts ranges from 8×10^{-5} to 6×10^{-4} Ω cm^2.

In contrast, Fig. 2c shows the I–V curves of 4-probe and 2-probe measurements of a nanobelt with high resistance Schottky contacts. The 2-probe I–V curve shows a strong rectifying behavior, clearly indicating the presence of Schottky barriers of different heights at the two contacts. However, the 4-probe I–V curve, which measures the actual resistance of the nanobelt between terminals B and C, is linear and indicates a much smaller resistance compared to the one measured by 2-probe. Therefore, the nature of the contacts has significant impact on the FET characteristics of the nanobelt devices.

The SnO_2 nanobelt devices with rectifying contacts have Schottky barrier FET characteristics while the devices with Ohmic contacts have intrinsic, channel-limited FET characteristics. A detailed discussion of the mechanisms and the characteristics of the SnO_2 nanobelt Schottky barrier FETs is provided in Supplementary data. Here we mainly focus on the intrinsic, channel-limited SnO_2 nanobelt FETs.

3.2. SnO_2 nanobelt FET characterization

SnO_2 nanobelt FETs with RuO_2/Au electrical contacts consistently exhibit typical n-channel depletion MOSFET characteristics. Fig. 3a is a schematic illustration of a single SnO_2 nanobelt FET with a circuit diagram showing the transistor measurement configuration. Fig. 3b and c shows the room temperature FET behavior of the four-terminal device shown in Fig. 1b, which has low-resistance Ohmic RuO_2/Au contacts. The two middle leads were used as the source and drain electrodes, and their contact resistances were monitored constantly under different gate bias by using 4-probe I–V measurements. The contact resistance increases by several orders of magnitude when V_{GS} decreases from 30 V to −30 V, which indicates that in the Ohmic contact case, there is still a small potential barrier with extremely narrow depletion width where an electron can tunnel through the barrier with ease (Although the work function of the contact material is larger than that of the SnO_2 nanobelt, in which case there should be no built-in barrier, the Fermi level at the surface of the real SnO_2 nanobelt is in reality probably pinned due to the high interface density in the gap.). The barrier height and the depletion width increase with the decrease of the gate voltage; hence, the contact resistance increased. However, the I–V curve between the source and drain electrode remains linear and non-rectifying at low biases and the contact resistance remains small (not more than 5% of the corresponding channel resistance at any given gate voltage) compared to that of the channel. Thus, the measured FET characteristics reflect the intrinsic response of the SnO_2 channel. The device exhibits typical n-channel depletion-mode FET characteristics. Fig. 3b shows the source-drain I–V curves at various gate voltages from +30 V (top) to −30 V (bottom) in steps of 2 V (the I_{DS}–V_{DS} curves for $V_{GS} < -24$ V cannot be seen in Fig. 3b due to the overlapping). In the "on" state, the I–V curves have a well-defined linear region at low biases, and the drain current saturates upon further increase in the bias due to the depletion of carriers around the drain electrode (the pinch-off effect).

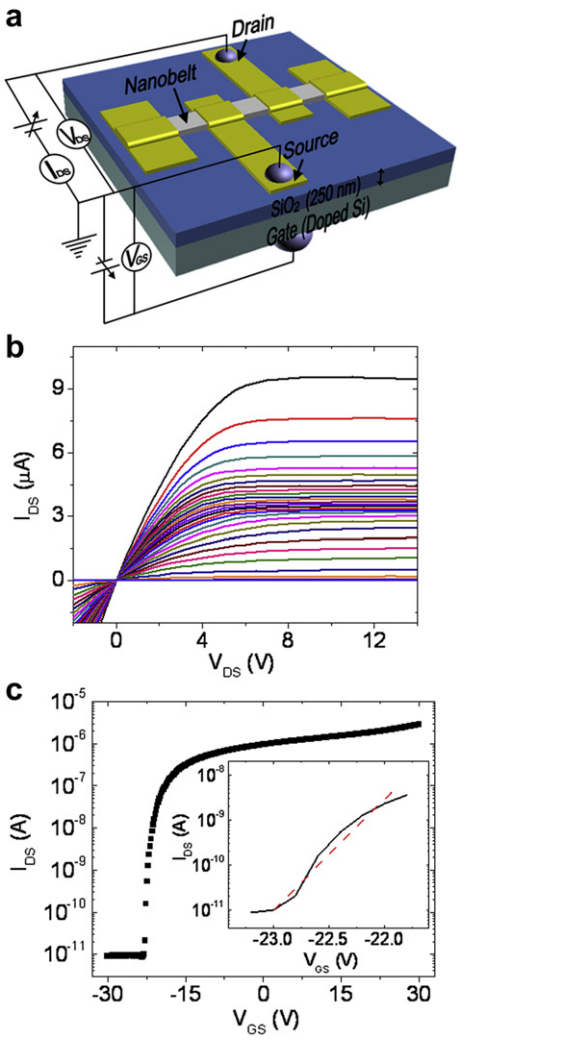

Fig. 3. The characteristics of an individual SnO_2 nanobelt based FET (field effect transistor) with Ohmic contacts. (a) A schematic illustration of a single SnO_2 nanobelt FET with a circuit diagram showing the transistor measurement configuration. (b) I_{DS}–V_{DS} plot when V_{GS} decreases from +30 V (top) to −30 V (bottom) in steps of 2 V (those I_{DS}–V_{DS} curves for $V_{GS} < -24$ V cannot be seen because they overlap). (c) I_{DS}–V_{GS} plot when $V_{DS} = 1$ V. Inset: a close-up view of the subthreshold region that highlights a subthreshold swing as small as 380 mV per decade.

The threshold voltage V_{th} for this device is about −23 V and the on/off ratio is over 10^5 as shown in Fig. 3c where the I_{DS} versus V_{GS} is plotted in logarithmic scale at a constant $V_{DS} = 1$ V (in the linear regime of the source-drain I–V). The inset of Fig. 3c shows a subthreshold swing, $S = \partial V_{GS}/\partial \log(I_{DS})$, which is about 380 mV per decade for this device. Considering the thickness of the gate oxide layer (250 nm SiO_2) used in this device, this value is quite encouraging.

We emphasize that because the FET action in the device is channel-limited, the calculated mobility is intrinsic to the SnO_2 nanobelt. The device also showed excellent stability, despite the sample to sample difference. Measurements before and after six months of storage in ambient air yielded the same transistor behavior with identical transfer characteristics and consistent transconductance values.

3.3. Mechanism and performance as hydrogen gas sensors

The conductivity of the nanobelt depends sensitively on the gas composition of the ambient environment. In light of the diffusion rate of the oxygen vacancy in the solid, these effects are thought to be due not to changes in bulk composition but to adsorption of gases on the surface of the nanobelt. The easily ionizable oxygen vacancies, V_0, defined as vacancies with two trapped electrons, that are formed when the surface of SnO_2 loses many of the lattice oxygen species, result in donor states that make the oxide nanobelt an extrinsic n-type semiconductor.

$$V_0^{++} + e^- \leftrightarrow V_0^+ \quad (3)$$

$$V_0^+ + e^- \leftrightarrow V_0 \quad (4)$$

During exposure to oxygen, the interaction with atmospheric oxygen with lattice vacancies leads to its ionosorption in molecular (O_2^-) and atomic (O^{2-} and O^-) forms [41,42]. The surface acceptor states are recreated and the electron concentration is reduced.

$$V_0 + O_2(\text{gas}) \leftrightarrow O_2(\text{molecular}) \quad (5)$$

$$O_2(\text{molecular}) + e^- \leftrightarrow O_2^-(\text{molecular}) \quad (6)$$

$$O_2^-(\text{molecular}) + e^- \leftrightarrow O_2^{2-}(\text{molecular}) \quad (7)$$

$$O_2^{2-}(\text{molecular}) \leftrightarrow 2O^-(\text{atomic}) \quad (8)$$

or

$$O_2^-(\text{molecular}) + e^- \leftrightarrow 2O^-(\text{atomic}) \quad (8')$$

$$O^-(\text{atomic}) + e^- \leftrightarrow O^{2-}(\text{atomic}) \quad (9)$$

It is worth noting that which oxygen species dominate depends on temperature and surface dopants. According to a literature survey by Barsan et al. [41], at low temperatures (below 150 °C) the molecular form dominates (equations (5)–(7)); while at high temperature (above 150 °C) the atomic form dominates (equations (8) and (9)).

The formation of these ions by oxygen adsorbed at the surface (gas/solid interface) extracts electrons from the bulk of the nanobelt. The oxygen can therefore be thought of as a trap for electrons from the bulk [43]. The presence of these species leads to the formation of an electron depletion layer at the surface of tin oxide. The electron depleted region, also called the space-charge layer, is a more resistive layer in comparison to the bulk nanobelt where the electron density is high. Since the non-stoichiometric tin oxide is an n-type semiconductor, the overall conductivity will decrease as the electrons are extracted.

When a reducing gas (e.g. H_2 or CO) is present in the atmosphere, it reacts with the negatively charged oxygen ion on the surface and is oxidized, and the electrons are released to the conduction band, which contributes to the increase in the channel conductance. It is worth noting that O_2^- is in general abundant at low temperatures and O^- is normally the active species at elevated temperatures [41]. Thus, in the case of room-temperature hydrogen sensing, hydrogen reacts with and removes the oxygen adsorbed on the metal oxide surface. At the same time, the free electrons are injected back in the conduction band, from the surface to the bulk, increasing the electron concentration and the conductance of the nanobelt channel. The reactions can be expressed as [42]:

$$2H_2(\text{gas}) + O_2^-(\text{molecular}) \leftrightarrow 2H_2O + e^- \quad (10)$$

The nanobelts have hydrogen-sensing capabilities with a significantly enhanced reaction time and high sensitivity at room temperature, which has been previously reported [19]. To follow up, we carried out experiments with lower concentrations of hydrogen and the 4-probe configuration in order to eliminate any electrical contribution from the metal/semiconductor contacts. Gas-sensing measurements were carried out in a quartz tube furnace using a constant flow-through method. The humidity within the quartz tube was 16%. The corresponding resistance changes were monitored and recorded using the sourcemeter and a Labview program with a standard 4-probe configuration. Fig. 4a shows the dynamic response–recovery curve of a SnO_2 nanobelt in ambient air and 0.2% hydrogen buffered in nitrogen at 25 °C. Note that in this set of experiments, the sensing gas is hydrogen buffered in nitrogen and the recovery gas is ambient air. The response time, defined as the time until a signal reaches 90% of its maximum response, is as short as 120 s and the sensitivity is 17.3% (conductance) and 14.7% (resistivity) for this sensor. The up-to-the-minute response time is possibly due to multiple surface reactions with dissociated hydrogen. Dissociated hydrogen can react with surface ionized oxygen species to form hydroxyl groups, which can further react to yield water vapor and electrons. Part of the contribution comes from hydroxyl groups bound to Sn atoms, the presence of which is confirmed by the IR studies [44]. Taking into account the dissociation of H_2,

$$H_2(\text{gas}) \leftrightarrow H + H \quad (11)$$

at lower temperature, atomic hydrogen reacts with chemisorbed oxygen species O_2^-:

$$2H + O_2^-(\text{molecular}) \leftrightarrow 2OH^-(\text{molecular}) \quad (12)$$

$$H + OH^-(\text{molecular}) \leftrightarrow H_2O(\text{gas}) + e^- \quad (13)$$

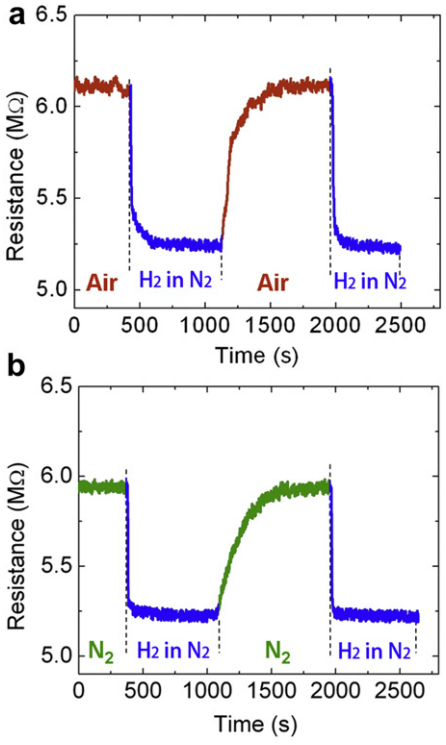

Fig. 4. Room-temperature sensing response of a four-terminal SnO_2 nanobelt device to 0.2% hydrogen buffered in nitrogen and recovery in (a) ambient air and (b) nitrogen.

As mentioned earlier, the results shown in Fig. 4a cannot exclude the effect of oxygen and humidity since the hydrogen was buffered in nitrogen and the recovery gas is actually ambient air. In order to verify that the resistance drop was due to the presence of hydrogen rather than the absence of oxygen, we switched the recovery gas from ambient air to pure nitrogen. In this way, we are sure that the only variable between sensing and recovery gases is the hydrogen composition. Fig. 4b shows the resistance in nitrogen and 0.2% H_2 at 25 °C. The contribution of nitrogen to the overall signal was estimated to be 3.3% (conductance) in this time period. Therefore, 80% of the increase of the conductance in the hydrogen sensing experiment can be attributed to the presence of hydrogen, although the nitrogen also contributes to the decrease in resistance. The sensor response time is also much faster (36 s) in response to hydrogen than when simply exposed to pure nitrogen. Besides the reduction of the pre-adsorbed oxygen species by the reducing gas, a possible interaction route for such effect of hydrogen in the absence of oxygen has been proposed by Hübner et al. [45] This mechanism [46] involves the dissociation of the hydrogen molecules followed by the adsorption of the hydrogen atoms onto the surface lattice oxygen ions (oxygen in the oxygen site with net charge of zero), so called "rooted" hydroxyl groups. The process can be described by the following equations:

$$H_2(\text{gas}) + 2O(\text{lattice}) \leftrightarrow 2OH^+(\text{lattice}) + 2e^- \quad (14)$$

The appearance of surface donors and their ionization results in the increase of the concentration of electrons in the conduction band and the decrease of the sensor resistance. This result and the results depicted later in Fig. 5 confirm that, near room temperature, introducing reducing gas will affect the resistance of the sensor faster and more significantly than just decreasing the oxygen pressure.

The thickness of the space charge layer is typically indicated by the Debye length of the electrons. The Debye screening length, λ_D, which for bulk SnO_2 is 4.39 nm at 300 K (with a carrier concentration value of 3.6×10^{18} cm^{-3} [47]), is defined as

$$\lambda_D = \sqrt{\frac{\varepsilon k_B T}{q^2 N_0}} \quad (15)$$

where ε is the static dielectric constant ($=13.5 \times 8.85 \times 10^{-12}$ F m^{-1} in SnO_2 [48]), k_B is the Boltzmann constant ($=1.38 \times 10^{-23}$ J K^{-1}), T is the absolute temperature ($=300$ K), q is the electrical charge of the carrier ($=1.6 \times 10^{-19}$ C), and N_0 is the carrier concentration ($=3.6 \times 10^{18}$ cm^{-3} [47]). According to the film classification described in the review paper by Barsan [41], the sensor is regarded as "thick layer" considering the fact that the space charge layer, where the electrons can switch back and forth between the surface states and the bulk, is only 1/10 of the total thickness (39 nm) of the nanobelt. The influence of surface phenomena will result in the modulation of the thickness of this conducting channel. However, the majority of the conduction is taking place in a core region which is unaffected by surface effects. This might be the reason for the limited performance of the sensor. The sensitivity can therefore be further improved by reducing the actual thickness of the nanobelt (close to the Debye screening length). Decreasing film thickness increases the sensor response because the fraction of material involved in the interaction with the gas is monotonously increased. Another way to improve the sensitivity of such transistor configuration is to apply a negative gate voltage to deplete the carriers (as a pinched-off FET) in the conducting channel, which is demonstrated by Cheng et al. in the experiments of hydronium ions (H_3O^+) sensing [20] and further reported by Gao et al. with the finding that the optimal sensitivity can be achieved in subthreshold regime with increased signal to noise level [49].

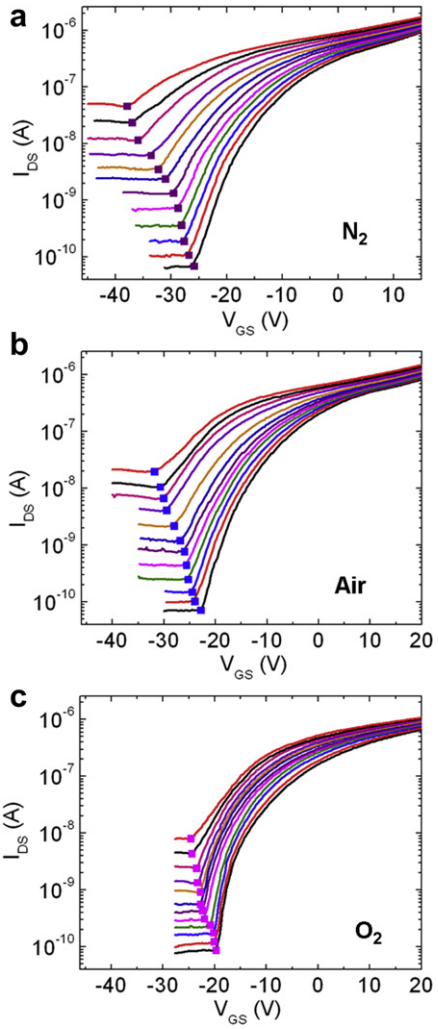

Fig. 5. The transfer characteristics of a channel-limited SnO_2 nanobelt FET ($V_{DS} = 1$ V) at 25 °C (bottom) to 135 °C (top) in steps of 10 °C in: (a) N_2, (b) ambient air and (c) O_2. These three atmospheres correspond to different oxygen concentrations of: 0%, 22% and 100%.

Despite the limited sensitivity, room temperature hydrogen sensing with intrinsic electrical response of SnO_2 nanobelt is attractive. The room temperature response, especially the fast response time, of the SnO_2 nanobelt sensor can be attributed to the large surface area to bulk volume ratio of the nanobelt, small lateral dimensions (thickness and width), and single crystalline morphology without any grain boundary. Compared with the polycrystalline and thick film SnO_2 sensor devices, in which only a small fraction of the species adsorbed near the grain boundaries is active in modifying the device electrical transport properties, almost all of the adsorbed species are active in producing a surface depletion layer in sensors based on single crystalline nanobelts. Secondly, commercial hydrogen semiconductor sensors often require substantial electric power to heat the working body of the sensing element up to a few hundred degrees Celsius. Search continues for decreasing the operation temperature of the sensors which could lead to decrease of power consumption and to possible use of portable battery supply. Another motivation to decrease the operating temperature is that the operation under high temperatures induces grain growth by coalescence and degrades the long-term stability of the materials and devices [50].

3.4. Gaseous modification of the electrical properties of a SnO_2 nanobelt FET

Most of the gas sensors reported previously employed the two-terminal geometry and thus could not reliably take advantage of the transistor characteristics as a means of gas sensing or determine the key electrical parameters of the nanobelts, e.g., effective carrier concentration and carrier mobility. Here, we demonstrate the extraction of the effective carrier concentration and the carrier mobility of the SnO_2 nanobelts and their variation with the ambient environment by analyzing the effects of surface modification on the intrinsic channel-limited FET transfer characteristics (with unambiguous exclusion of any contact effects).

Fig. 5a–c shows the transfer characteristics of a SnO_2 nanobelt FET (when $V_{DS} = 1$ V, in linear I_{DS}–V_{DS} region) at temperatures from 25 °C to 135 °C in steps of 10 °C in N_2, ambient air and O_2 respectively. These three different atmospheres correspond to three different oxygen concentrations: 0, 22% and 100%. The response times of the device to the above gases are very long (over 20 min) compared to that for hydrogen.

First, the effective field-effect carrier mobility, μ_{eff}, of the FET, can be estimated from

$$g_m = \frac{Z\mu_{eff}C_O V_{DS}}{L}, \quad (16)$$

where Z is the channel width (corresponding to the nanobelt width of 150 nm), L is channel length (corresponding to the electrode separation of 4 μm), C_O is oxide capacitance per unit area. Assuming a model of two infinite parallel plates, for the 250 nm thick SiO_2 substrate, $C_O = 1.4 \times 10^{-4}$ F m^{-2}. However, due to the fact that the width of the nanobelt is close to the value of the thickness of the dielectric layer, where the fringing effect cannot be ignored, the infinite parallel plates model is clearly inadequate. To account for the highly non-uniform electric field between the conducting nanobelt (channel) and the doped Si (gate), we calculated the capacitance using integration of the electric field energy density $W_e (C = 2W_e/U_{gs}^2)$ and integration of the induced charge density on both electrode ($C = Q/U_{gs}$) using COMSOL MULTIPHYSICS v3.2; similar calculation methods have been described previously [51]. See Supplementary data for detailed simulation and calculation of the capacitance. A final C_O value of 2.7×10^{-4} F m^{-2} was obtained and used to calculate the effective mobility μ_{eff}.

Second, from the equation

$$n_e = \frac{|V_{th}| \cdot C}{q \cdot t \cdot Z \cdot L} \quad (17)$$

where V_{th} is threshold voltage, q the electron charge, t the thickness of nanobelt, Z the width, and L the active length, we can calculate the effective carrier concentration from the value of the threshold voltage.

Using the precise measurements of I_{DS}–V_{GS}, we calculated the transconductance. At $V_{GS} = 0$ V and a temperature of 75 °C, the transconductance, g_m, decreases slightly from 3.19×10^{-8} S (N_2) to 2.55×10^{-8} S (ambient air) and 1.92×10^{-8} S (O_2) with increasing oxygen concentrations. At a negative gate bias $V_{GS} = -25$ V and the same temperature, the difference in transconductance increases (2.28×10^{-12} S in N_2, 1.89×10^{-9} S in ambient air, and 1.04×10^{-8} S in O_2). The transconductance values at $V_{GS} = 0$ V were recorded in these three gaseous environments and the corresponding effective carrier mobilities μ_{eff} (calculated using equation (16)) were plotted as a function of temperature (Fig. 6a). The effective carrier mobility value is greater when the device is exposed to an environment with less oxygen. The mobility is probably determined by competition between phonon scattering and ionized impurity scattering. Adsorption of oxygen will introduce more defects or impurities in the crystal, which lead to more scattering of the carrier and reduction in mobility. The effective carrier mobility does not change much with the temperature, probably due to the narrow temperature range.

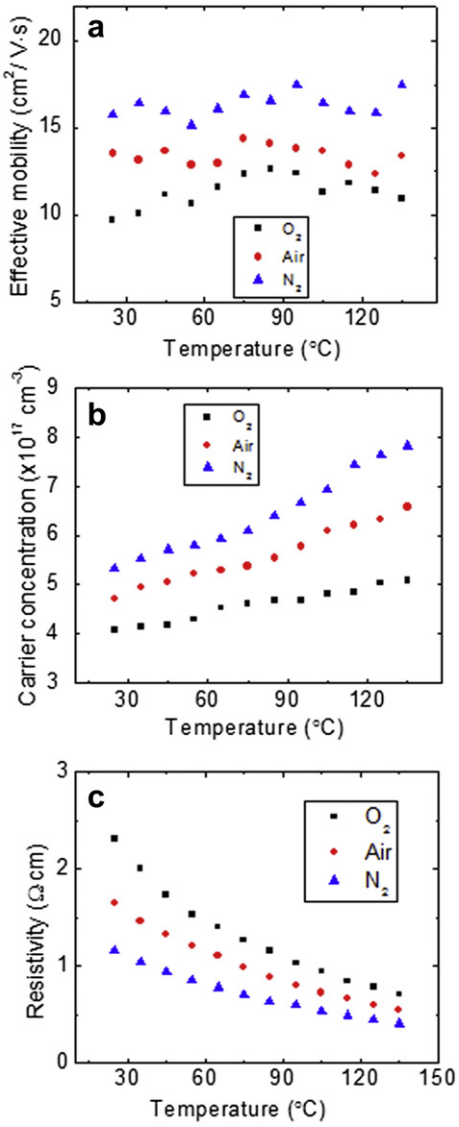

Fig. 6. (a) The effective carrier mobility μ_{eff} versus temperature in O_2, ambient air and N_2. (b) The effective carrier concentration n_e versus temperature in O_2, ambient air and N_2. (c) Resistivity versus temperature in O_2, ambient air and N_2.

The threshold voltages, V_{th}, of the device under different conditions are indicated in Fig. 5 as solid squares. The effective carrier concentrations, n_e, of the nanobelt at various temperatures under different gaseous environments were calculated using equation (16). Fig. 6b shows n_e versus temperature in O_2, ambient air, and N_2. Obviously, as the temperature increases, the absolute value of the threshold voltage (effective carrier concentration) increases. The effective carrier concentration value is larger when the device is exposed to an environment with a smaller oxygen concentration. Fig. 6c shows the resistivity of the nanobelt (at $V_{GS} = 0$ V) as a function of temperature (within the 25–135 °C range). Obvious decrease of the resistivity with increasing temperature and the higher resistivity at higher oxygen concentration are observed. These observations are consistent with the

modification of the oxygen vacancies and the mechanism described in Section 3.3. Within our experimental temperature range, higher oxygen concentration leads to fewer carriers and higher resistivity of the SnO_2 nanobelt while the mobility remains at the same level. Also, notice that as the temperature increases, the on/off ratio decreases because the extra carriers make the device harder to deplete and result in a larger "off" current.

4. Conclusion

In conclusion, we have performed a comprehensive study on the intrinsic electrical properties of single-crystalline SnO_2 nanobelts by standard 4-probe measurements. The channel-limited SnO_2 nanobelt FETs with RuO_2/Au Ohmic contact exhibit excellent transistor characteristics. We have also demonstrated that such SnO_2 nanobelt FET devices are promising room temperature hydrogen gas sensor due to its high surface to volume ratio for effective oxygen diffusion. The sensitivity can be further improved by reducing the thickness of the nanobelt down to the Debye screening length, which is about 4 nm according to our calculation. The resistivity, effective carrier mobility and carrier concentration of the nanobelt were obtained in different oxygen concentration environments. The results provides better understanding toward the electrical properties and sensing mechanism of the one dimensional SnO_2 nanostructures and demonstrate the possibility of synthesizing room temperature chemo-resistive gas sensors based on SnO_2 nanobelts.

Competing interests

The authors declare that they have no competing interests.

Acknowledgment

The authors thank Dr. Olaf Wunnicke for valuable discussions of the finite element method of simulating the electrical field of the device and Drs. Stephan von Molnár and Cong Ren for assistance with the electrical measurements. This work was supported by NSF NIRT Grant No. ECS-0210332 and an FSU Research Foundation PEG grant.

Appendix A. Supplementary data

Supplementary data associated with this article can be found in the online version, at http://dx.doi.org/10.1016/j.matchemphys.2012.09.037.

References

[1] M.S. Arnold, P. Avouris, Z.W. Pan, Z.L. Wang, Field-effect transistors based on single semiconducting oxides nanobelts, J. Phys. Chem. B 107 (2003) 659–663.
[2] C. Li, D.H. Zhang, X.L. Liu, S. Han, T. Tang, J. Han, C. Zhou, In_2O_3 nanowires as chemical sensors, Appl. Phys. Lett. 82 (2003) 1613–1615.
[3] Y.W. Heo, D.P. Norton, L.C. Tien, Y. Kwon, B.S. Kang, F. Ren, S.J. Pearton, J.R. LaRoche, ZnO nanowire growth and devices, Mater. Sci. Eng., R 47 (2004) 1.
[4] A. Kolmakov, M. Moskovits, Chemical sensing and catalysis by one-dimensional metal-oxide nanostructures, Annu. Rev. Mater. Res. 34 (2004) 151–180.
[5] A. Kolmakov, D.O. Klenov, Y. Lilach, S. Stemmer, M. Moskovits, Enhanced gas sensing by individual SnO_2 nanowires and nanobelts functionalized with Pd catalyst particles, Nano Lett. 5 (2005) 667–673.
[6] Z.W. Pan, Z.R. Dai, Z.L. Wang, Nanobelts of semiconducting oxides, Science 291 (2001) 1947–1949.
[7] Z.L. Wang, Z.W. Pan, Nanobelts of semiconductive oxides: a structurally and morphologically controlled nanomaterials system, Int. J. Nanosci. 1 (2002) 41–51.
[8] Z.R. Dai, J.L. Gole, J.D. Stout, Z.L. Wang, Tin oxide nanowires, nanoribbons, and nanotubes, J. Phys. Chem. B 106 (2002) 1274–1279.
[9] Y.W. Heo, V. Varadarajan, M. Kaufman, K. Kim, D.P. Norton, F. Ren, P.H. Fleming, Site-specific growth of Zno nanorods using catalysis-driven molecular-beam epitaxy, Appl. Phys. Lett. 81 (2002) 3046.
[10] P. Yang, H. Yan, S. Mao, R. Russo, J. Johnson, R. Saykally, N. Morris, J. Pham, R. He, H.-J. Choi, Controlled growth of ZnO nanowires and their optical properties, Adv. Funct. Mater. 12 (2002) 323–331.
[11] E. Comini, G. Faglia, G. Sberveglier, Z. Pan, Z.L. Wang, Stable and highly sensitive gas sensors based on semiconducting oxide nanobelts, Appl. Phys. Lett. 81 (2002) 1869–1871.
[12] Z. Fan, D. Wang, P.C. Chang, W.Y. Tseng, J.G. Lu, ZnO nanowire field-effect transistor and oxygen sensing property, Appl. Phys. Lett. 85 (2004) 5923–5925.
[13] H.T. Wang, B.S. Kang, F. Ren, L.C. Tien, P.W. Sadik, D.P. Norton, S.J. Pearton, Hydrogen-selective sensing at room temperature with ZnO nanorods, Appl. Phys. Lett. 86 (2005) 243503.
[14] A. Tricoli, M. Righettoni, A. Teleki, Semiconductor gas sensors: dry synthesis and application, Angew. Chem., Int. Ed. 49 (2010) 7632–7659.
[15] D.Z.Z. Liu, S. Han, C. Li, T. Tang, W. Jin, X. Liu, B. Lei, C. Zhou, Laser ablation synthesis and electron transport studies of tin oxide nanowires, Adv. Mater. 15 (2003) 1754–1757.
[16] S.V. Kalinin, J. Shin, S. Jesse, D. Geohegan, A.P. Baddorf, Y. Lilach, M. Moskovits, A. Kolmakov, Electronic transport imaging in a multiwire SnO_2 chemical field-effect transistor device, J. Appl. Phys. 98 (2005) 044503–044508.
[17] Y.Z.A. Kolmakov, G. Cheng, M. Moskovits, Detection of CO and O_2 using tin oxide nanowire sensors, Adv. Mater. 15 (2003) 997–1000.
[18] A. Maiti, J.A. Rodriguez, M. Law, P. Kung, J.R. McKinney, P. Yang, SnO_2 nanoribbons as NO_2 sensors: insights from first principles calculations, Nano Lett. 3 (2003) 1025–1028.
[19] L.L. Fields, Y. Cheng, P. Xiong, J.P. Zheng, Room-temperature low-power hydrogen sensor based on a single tin dioxide nanobelt, Appl. Phys. Lett. 88 (2006) 263102.
[20] Y. Cheng, C.S. Yun, R.S. Yang, J.P. Zheng, Z.L. Wang, G.F. Strouse, P. Xiong, Mechanism and optimization of pH sensing with single SnO_2 nanobelt, Nano Lett. 8 (2008) 4179–4184.
[21] C. Baratto, S. Todros, E. Comini, G. Faglia, M. Ferroni, G. Sberveglieri, G. Andreano, L. Cellai, A. Flamini, G. Marrazza, A. Nannini, G. Pennelli, M. Piotto, SnO_2 nanowire bio-transistor for electrical DNA sensing, in: IEEE SENSORS 2007 Conference (2007). pp. 1132–1135.
[22] Y. Cheng, K.-S. Chen, N.L. Meyer, J. Yuan, L.S. Hirst, P.B. Chase, P. Xiong, Functionalized SnO_2 nanobelt field-effect transistor sensors for label-free detection of cardiac troponin, Biosens. Bioelectron. 26 (2011) 4538–4544.
[23] Y. Lilach, J.-P. Zhang, M. Moskovits, A. Kolmakov, Encoding morphology in oxide nanostructures during their growth, Nano Lett. 5 (2005) 2019–2022. http://dx.doi.org/10.1021/nl051543f.
[24] F. Hernandez-Ramirez, A. Tarancon, O. Casals, J. Rodriguez, A. Romano-Rodriguez, J.R. Morante, S. Barth, S. Mathur, T.Y. Choi, D. Poulikakos, V. Callegari, P.M. Nellen, Fabrication and electrical characterization of circuits based on individual tin oxide nanowires, Nanotechnology 17 (2006) 5577–5583.
[25] W. Göpel, K.D. Schierbaum, SnO_2 sensors: current status and future prospects, Sens. Actuators, B: Chem. 26 (1995) 1–12.
[26] P. Andrei, L.L. Fields, J.P. Zheng, Y. Cheng, P. Xiong, Modeling and simulation of single nanobelt SnO_2 gas sensors with FET structure, Sens. Actuators, B: Chem. 128 (2007) 226–234.
[27] G. Korotcenkov, Gas response control through structural and chemical modification of metal oxide films: state of the art and approaches, Send. Actuators, B: Chem. 107 (2005) 209–232.
[28] Y. Cheng, L.L. Fields, R.S. Yang, J.P. Zheng, Z.L. Wang, P. Xiong, Intrinsic characteristics of semiconducting oxide nanobelt field-effect transistors, Appl. Phys. Lett. 89 (2006) 093114.
[29] H.K. Henisch, Semiconductor Contacts: An Approach to Ideas and Models, Clarendon Press, Oxford, 1984.
[30] E.H. Rhoderick, R.H. Williams, Metal/semiconductor Contacts, Clarendon Press, Oxford, 1988.
[31] Contacts to Semiconductors: Fundamentals and Technology, William Andrew Publishing/Noyes, Park Ridge, NJ, 1993.
[32] L.J. Brillson, Surfaces, Interfaces: Atomic-scale Structure, Band Bending and Band Offsets, in: P.T. Landsberg (Ed.), Handbook on Semiconductors, North-Holland, Amsterdam, 1992, pp. 281–417.
[33] S.M. Sze, Physics of Semiconductor Device, second ed., John Wiley and Sons, New York, 2002.
[34] J. Singh, Semiconductor Devices: Basic Principles, John Wiley and Sons, New York, 2001.
[35] J.F. Geiger, K.D. Schierbaum, W. Gopel, Surface spectroscopic studies on Pd-doped SnO_2, Vacuum 41 (1990) 1629–1632.
[36] L. Solymar, D. Walsh, Electrical Properties of Materials, sixth ed., Oxford Science Publications, Oxford, UK, 1990.
[37] J.P. Zheng, P.J. Cygan, T.R. Jow, Hydrous ruthenium oxide as electrode material for electrochemical capacitors, J. Electrochem. Soc. 142 (1995) 2695.
[38] Q.X. Jia, X.D. Wu, S.R. Foltyn, A.T. Findikoglu, R. Tiwari, J.P. Zheng, T.R. Jow, Heteroepitaxial growth of highly conductive metal–oxide RuO_2 thin films by pulsed laser deposition, Appl. Phys. Lett. 67 (1995) 1677.
[39] E.V. Jelenkovic, K.Y. Tong, Thermally grown ruthenium oxide thin films, J. Vac. Sci. Technol., B 22 (2004) 2319–2325.
[40] H.C. Zhong, G. Heuss, V. Misra, H.F. Luan, C.H. Lee, D.L. Kwong, Characterization of RuO_2 electrodes on Zr silicate and ZrO_2 dielectrics, Appl. Phys. Lett. 78 (2001) 1134–1136.

[41] N. Barsan, U. Weimar, Conduction model of metal oxide gas sensors, J. Electroceramics 7 (2001) 143–167.
[42] A. Gurlo, R. Riedel, In situ and operando spectroscopy for assessing mechanisms of gas sensing, Angew. Chem., Int. Ed. 46 (2007) 3826–3848.
[43] P.T. Moseley, Solid state gas sensors, Meas. Sci. Technol. 8 (1997) 223–237.
[44] E.W. Thornton, P.G. Harrison, Tin oxide surfaces. Part 3.—Infrared study of the adsorption of some small organic molecules on tin(IV) oxide, J. Chem. Soc., Faraday Trans. 1: Phys. Chem. Condens. Phases 71 (1975) 2468–2477.
[45] M. Hubner, R.G. Pavelko, N. Barsan, U. Weimar, Influence of oxygen backgrounds on hydrogen sensing with SnO_2 nanomaterials, Sens. Actuators B: Chem. 154 (2011) 264–269.
[46] V.E. Henrich, P.A. Cox, The Surface Science of Metal Oxides, Cambridge University Press, Cambridge, UK, 1994.
[47] H. Ogawa, M. Nishikawa, A. Abe, Hall measurement studies and an electrical conduction model of tin oxide ultrafine particle films, J. Appl. Phys. 53 (1982) 4448–4455.
[48] R. Summitt, Infrared absorption in single-crystal stannic oxide: optical lattice-vibration modes, J. Appl. Phys. 39 (1968) 3762–3767.
[49] X.P.A. Gao, G. Zheng, C.M. Lieber, Subthreshold regime has the optimal sensitivity for nanowire FET biosensors, Nano Lett. 10 (2009) 547–552.
[50] E. Comini, G. Sberveglieri, Metal oxide nanowires as chemical sensors, Mater. Today 13 (2010) 28–36.
[51] O. Wunnicke, Gate capacitance of back-gated nanowire field-effect transistors, Appl. Phys. Lett. 89 (2006) 083102.